IEEE Access
Multidisciplinary | Rapid Review | Open Access Journal

Received October 10, 2021, accepted October 24, 2021, date of publication November 1, 2021, date of current version November 8, 2021.

Digital Object Identifier 10.1109/ACCESS.2021.3124614

Advanced Decoupling Techniques for Grid-Connected Inverters With Multiple Inputs

GUANHONG SONG[1], (Member, IEEE), BO CAO[1], (Member, IEEE), LIUCHEN CHANG[1], (Senior Member, IEEE), AND RIMING SHAO[2], (Member, IEEE)

[1]Emera and NB Power Research Centre for Smart Grid Technologies, University of New Brunswick, Fredericton, NB E3B 5A3, Canada
[2]Alpha Technologies Inc., Bellingham, WA 98226, USA

Corresponding author: Bo Cao (b.cao@unb.ca)

This work was supported in part by Emera Inc. and in part by the Atlantic Innovation Fund for the research.

ABSTRACT The parallel connection of multiple distributed energy resources with a common DC-link structure is typically used in grid-connected applications which enables flexible operation maximizing power production of the inverter system under various operation conditions. However, it has brought drawbacks for DC-link power decoupling with the requirement of a larger capacitor bank, faster voltage regulation, etc., to maintain a constant DC-link voltage which increases the overall size and cost. In this paper, a DC-link decoupling technique using a nonlinear control algorithm is proposed to perform rapid DC-link voltage regulation for multi-input grid-connected inverters. With the implementation of a nonlinear observer, the power fed into the DC-link from multiple inputs is estimated by the proposed control algorithm and can be rapidly compensated by the inverter minimizing the DC-link voltage fluctuation. The effectiveness of the proposed nonlinear power decoupling control algorithm is verified by comparing the DC-link performance with a conventional control algorithm through both simulation results on a MATLAB platform and experimental verification on a grid-connected inverter prototype.

INDEX TERMS DC-AC power converters, observers, nonlinear control systems, feedforward systems.

I. INTRODUCTION

With increasing environmental concerns, electricity demand and advancement of power electronics technologies, distributed energy resources (DERs) have been experiencing significant growth during last decades [1]–[3] and are playing more important roles in modern smart grid systems. Among all DERs, renewable sources such as wind [4] and photovoltaics [5] have already been key parts in distributed power generation systems. With the development of battery technologies, battery based energy storage systems[6] as well as electrical vehicles (EVs) [7] have also become essential elements in distributed energy resources. In order to regulate the operation of these DERs, maximize their power generation, perform power conversion meeting grid interconnection standards, grid-connected inverters are therefore required as the most critical interface between these DERs and power grids [8]–[11]. Meanwhile, considering the fact that these DERs have different power generation characteristics, multi-input grid-connected inverter is therefore used to coordinate the operation through a common DC-link structure [12]. Compared with conventional systems where each energy resource is equipped with a grid-connected inverter, the multi-input inverter has its advantages, such as: minimizing the use of switching components so that energy losses during power conversion is reduced; and flexible operation with internal power sharing capability which enables steady power generation to the utility grid even under the extreme input conditions, etc.

However, due to the existence of uncertainties in these DERs [13], the power production may change violently which causes voltage fluctuations on DC-link and degrade the operation of the system. According to [14], the grid current can be severely affected by the DC-link voltage causing high current total harmonics distortion (THD) issue. As also presented in [15], low frequency DC-link voltage fluctuations may show up in the grid current due to high bandwidth of the current controller causing oscillations in the output power. In order to minimize the impact of the rapid DER power variations over DC-link, a large DC-link capacitor is usually required to compensate these power variations, which, in return, decreases system power density and increases the size & cost of the inverter system [16]. Apart from large DC-link capacitor, the DC-link voltage controller

The associate editor coordinating the review of this manuscript and approving it for publication was Yuh-Shyan Hwang.

is also designed to reduce these voltage fluctuations. As stated in [17], the DC-link capacitance required to achieve a given maximum voltage overshoot can be reduced by maximizing voltage control bandwidth. In other word, both the DC-link capacitor and DC-link voltage fluctuations can be minimized with a properly designed DC-link voltage control loop, which is set as the fundamental when developing the proposed power decoupling technique.

In recent literature, the master-slave control method [18], feedforward compensation methods [19], [20] and deadbeat control algorithm [21] have found their place with fast voltage regulation performance and high bandwidth so that DC-link voltage variation can be minimized for inverter systems. However, all of these methods require additional communication and data exchange capabilities between DER-side converters and grid-side inverter which increases overall complexity of the control design procedure and limits plug-and-play capability for future system extension.

Meanwhile, the dual-loop control algorithms have been implemented in recent inverter applications [22], [23] for its simple controller design procedure and communication-less control environment so that plug-and-play operation of the multi-input inverter system is enabled. Among the dual-loop control methods, the proportional-integral (PI) control algorithm has already been widely used in practical applications [24], [25]. However, the performance of these PI controllers heavily relies on the system parameters and controller design accuracy which cannot resolve the conflicts between the steady-state performance and transient behavior. Facing the tradeoff between steady-state behavior and transient performance, some improved PI control methods were introduced into the power converter system. In [26], an adaptive PI algorithm based-on discrete-time model was presented where the proportional and integral gains of the controller were determined using an adaptive process aiming to minimize the DC-link voltage fluctuation during power transience. Nevertheless, an adaptive nonlinear PI control method was introduced in [27] where two PI controllers, one tuned for steady-state operation while the other one tuned with fast transient performance, were combined as a Takagi-Sugeno-type controller. These two PI controllers had adaptive control gains depending on the error of the measured and reference DC-link voltage so that both the steady-state and transient performance could be satisfied. However, these proposed controllers [26], [27] also shared the drawback of the PI method which was sensitive to parameter variations particularly for the transient performances.

Apart from dual-loop controllers, other control algorithms can also be introduced to multi-input inverter systems. Hysteresis voltage control algorithm was proposed in [28] for three-phase power inverter systems. Although the hysteresis controller is more robust as it is completely parameter-independent, it also shows a poor dynamic performance during power transients with small control bandwidth and the DC-link voltage kept oscillating within the hysteresis band. In [29], a nonlinear slide-mode controller (SMC) was implemented to replace the PI controller to achieve better dynamic responses as well as to compensate system uncertainties, such as parameter variations. Even though the presented method showed a faster transient behavior compared to PI controllers, the voltage ripples introduced by the nonlinear characteristics of the SMC resulted in poor steady-state performance. In [30], a state-space control algorithm was designed so that both the DC-link voltage and grid current are controlled based on one full-state differential equation. Similar methods, such as predictive control method [31] and SMC method [32], have also been developed with high controller bandwidth and fast DC-link voltage regulation based on system state-space model. Computation complexity and parameter sensitivity are the major drawbacks of these state-space controllers [30]–[32]. Load estimation methods, as improvement methods based on feed-forward compensation, were introduced in [33]–[36] where the transient behaviors of the control system were improved with by estimating the input current/power to the DC-link. Since no data exchange is required by these methods, they can be easily implemented in the multi-input inverter with minor modifications. However, the estimation technique presented in these literatures were all originated for steady-state estimations. In a practical multi-input inverter, due to the randomness nature of these DERs the existence of rapid DC-link input power variation results to huge estimation mismatches, which degrades the performance of these observers during power transience causing large DC-link voltage fluctuations.

In order to adopt the operation of these power estimation methods in the multi-input inverters, an improved power decoupling algorithm based on nonlinear power estimation is proposed and analyzed in this paper to reduce estimation errors and to minimize DC-link voltage fluctuations during rapid power variations. The main contributions of this paper can be summarized as follows:

1. A power decoupling algorithm using a nonlinear observer is proposed for the grid-side inverter which regulates the DC-link voltage under rapid input variations from multiple input DERs.
2. Detailed mathematical design, analysis, and parameter selection of the proposed nonlinear observer using Lyapunov stability theory are provided for understanding the proposed algorithm.

The effectiveness of the proposed nonlinear control algorithm is verified by both simulation and experimental comparison with a typical linear observer-based reference method presented in [33] from recent literature.

This paper is an extended and revised version of conference paper [37] with extended analysis, development and explanation on the design of the nonlinear observer along with extended experimental comparison with a reference method. The remainder of this paper is organized as follows: the detailed mathematical analysis of the multi-input inverter is described in Section II. The proposed nonlinear DC-link voltage control algorithm is presented and explained in detail

in Section III. Simulation and experimental validations are presented and discussed in Section IV and the conclusion is provided in Section V.

II. MULTI-INPUT INVERTER SYSTEM

In order to design the proposed power decoupling control algorithm on a practical inverter system with multiple input, the characteristics of the inverter system as well as the mathematical DC-link model are first discussed in this section. A typical three-phase DER-based multi-input inverter system is presented in Fig. 1, where multiple distributed energy resources and their power converters are connected to the utility grid through a common DC-link with a shared grid-connected inverter.

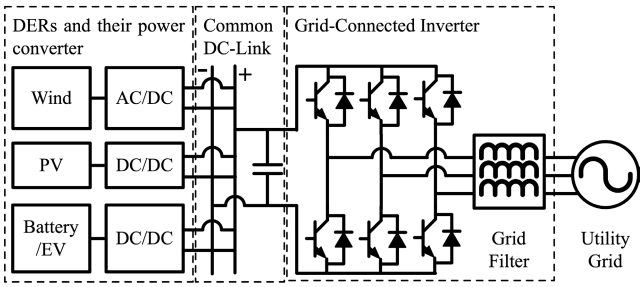

FIGURE 1. Typical structure for three-phase hybrid DER power conversion system.

During normal conditions, these DERs are either operated under their maximum power point tracking (MPPT) operations (for wind, PV) or regulated to follow preset power trajectories (for battery storage, EV). And the power production/consumption from these resources can be internally shared through the common DC-link. However, the interconnection of these resources has also brought severe drawbacks on the DC-link due to stack of energy uncertainties when the power production/consumption from these resources changes violently. As discussed in [28] and [38], the DC-link capacitor is used as power decoupling storage elements to balance power difference between DER-side converters and the grid-side inverter. Through maintaining a constant DC-link voltage, the operation of both converters and the inverter can be fully decoupled without interfering with each other which forms the fundamental of communication less operation of the inverter with multiple inputs. Here, all the investigated DER sources are operated with their individual MPPT algorithms and power trajectories for their power production, connected as inputs of the DC-link and no additional high-level power management devices are required with power decoupling from DC-link capacitors.

Therefore, in order to compensate the drawback in the multi-input inverter system with the advanced power decoupling control algorithm, the DC-link model which reflects the characteristics of this inverter system is required to design such a controller. Even though the DC-link can be built with a complicated mathematical model with its internal resistance and leakage, as discussed in [15], the DC-link energy balance model is sufficient when modeling the power flows within the inverter system. Therefore, the DC-link model for the DER-based multi-input inverter system can be formulated as (1) for further simplification:

$$\frac{1}{2}C_s\frac{dV_{dc}^2}{dt} = p_{in1} + p_{in2} + \cdots + p_{inN} - p_{out} - p_{loss} \tag{1}$$

where V_{dc} represents the DC-link voltage, C_s is the capacitance of the DC-link capacitor, p_{in1}, p_{in2} and p_{inN} represent the input power from each of the Nth DER-side converter to the DC-link, p_{out} is the output power from the grid-side inverter and p_{loss} is the power losses across the system. It is worth to point out that this DC-link model (1) is valid for the system whose grid-current controller behave as an ideal second-order low-pass filter and has a much higher bandwidth than the DC-link voltage control loop. Therefore, the performance of the inner current loop can be neglected in the model (1).

Equation (1) can be further extended as (2), where $p_{in}^N = p_{in1} + p_{in2} + \cdots + p_{inN}$, $p_{out}^N = p_{out}$, and $\dot{p}_{in}^N = k$ represents that either the input power to the DC-link is constant when $k = 0$, or the input power to the DC-link is continuously changing when $k \neq 0$. In other word, k is the changing rate of the input power to DC-link and, for a practical system, this k has a bounded range of $-k_{max} < k < k_{max}$ where k_{max} is the maximum power changing rate under the worst-case scenario of the multiple DERs. The power losses p_{loss} is neglected since it is too small compared to the power flow through the DC-link capacitors.

$$\begin{aligned} \frac{1}{2}C_s\frac{dV_{dc}^2}{dt} &= p_{in}^N - p_{out}^N \\ \dot{p}_{in}^N &= k. \end{aligned} \tag{2}$$

Therefore, the modified DC-link model (2) can be used for the nonlinear observer design presented in the next step.

III. ADVANCED DC-LINK DECOUPLING TECHNIQUE

The most critical aspect in minimizing the DC-link voltage fluctuation lies in rapid estimation of the input power. Therefore, details of the proposed nonlinear observer are first introduced in this section with detailed observer design, parameter selection, performance, and stability analysis. Then the proposed control algorithm is developed based on this nonlinear observer.

A. DESIGN OF THE PROPOSED NONLINEAR OBSERVER

Based on DC-link model (2), a modified state-space DC-link model specifically for the power transient period is presented below as (3) for the design of the proposed nonlinear DC-link voltage control algorithm. Here, the nonlinear observer is built under the worst-case scenario that the input power is changed at its maximum rate $k = k_{max}$. In other words, if the DC-link voltage fluctuation can be maintained within a desired value under the worst-case scenario, any other operation will result in better performance with smaller

voltage fluctuation.

$$\begin{aligned} \dot{x} &= Ax + Bu + K_k \\ y &= Cx \end{aligned} \tag{3}$$

where $x = \begin{bmatrix} x_1 & x_2 \end{bmatrix} = \begin{bmatrix} V_{dc}^2 & p_{in}^N \end{bmatrix}$, y is the system output, $u = p_{out}^N$ is the control input,

$$A = \begin{bmatrix} 0 & \frac{2}{C_s} \\ 0 & 0 \end{bmatrix}, \quad B = \begin{bmatrix} -\frac{2}{C_s} \\ 0 \end{bmatrix},$$
$$C = \begin{bmatrix} 1 & 0 \end{bmatrix}, \quad K_k = \begin{bmatrix} 0 \\ k_{max} \end{bmatrix}.$$

Therefore, the proposed nonlinear power observer can be built based on the state-space model (3) and is formulated as (4):

$$\begin{aligned} \dot{\hat{x}} &= A\hat{x} + Bu + \begin{bmatrix} -h_1\sqrt{|\hat{y} - y|} * \mathrm{sgn}(\hat{y} - y) \\ -h_2\sqrt{|\hat{y} - y|} * \mathrm{sgn}(\hat{y} - y) \end{bmatrix} \\ \hat{y} &= C\hat{x} \end{aligned} \tag{4}$$

where $\hat{x}$ is the estimated value of state x, $\hat{y}$ is the estimated value of output y, h_1 and h_2 are the gains of the nonlinear observer with $h_1 > 0$ and $h_2 > 0$.

By subtracting (3) into (4) and replacing output y with Cx, the error model of the nonlinear observer is obtained in (5) for stability analysis:

$$\begin{aligned} \dot{e}_1 &= -h_1 |e_1|^{\frac{1}{2}} \mathrm{sgn}(e_1) + \frac{2}{C_s} e_2 \\ \dot{e}_2 &= -k_{max} - h_2 |e_1|^{\frac{1}{2}} \mathrm{sgn}(e_1) \end{aligned} \tag{5}$$

where $e_1 = \hat{x}_1 - x_1$ and $e_2 = \hat{x}_2 - x_2$ are the errors between estimated state and actual state, respectively.

Considering the fact that the nonlinear observer is built under rapid input power variations, the steady-state operation does not exist during these operation conditions. Therefore, the stability analysis of the proposed observer mainly focuses on transient stability. In order to verify the transient stability of the proposed nonlinear observer as well as to develop general rules in selection of the observer gains h_1 and h_2, a general Lyapunov function is proposed in (6):

$$V(e_1, e_2) = ae_1^2 - be_1e_2 + ce_2^2 \tag{6}$$

where a, b and c are the parameters of the general Lyapunov function which are selected based on certain rules and will be explained further in this paper.

According to Lyapunov stability theory, the proposed observer is stable when there exists a positive definite Lyapunov function while its derivative is a negative semi-definite function. The Lyapunov function in (6) can be transform into (7) for detail analysis:

$$\begin{aligned} V(e_1, e_2) &= ae_1^2 - be_1e_2 + ce_2^2 \\ &= a(e_1^2 - 2\frac{b}{2a}e_1e_2 + (\frac{b}{2a}e_2)^2) - \frac{b^2}{4a}e_2^2 + ce_2^2 \\ &= a(e_1 - \frac{b}{2a}e_2)^2 + \left(c - \frac{b^2}{4a}\right)e_2^2 \end{aligned} \tag{7}$$

In order to obtain a positive definite of the Lyapunov function $V(e_1, e_2)$, following rules must be fulfilled:

$$\begin{aligned} &(\mathbf{RULE1}) a > 0 \\ &(\mathbf{RULE2}) c > \frac{b^2}{4a} > 0 \end{aligned}$$

There exist reasonable parameters a, b and c to guarantee a positive definite Lyapunov function $V(e_1, e_2)$.

Meanwhile, the negative semi-definite property of the derivative of the Lyapunov function $\dot{V}(e_1, e_2)$ also needs to be fulfilled. The partial derivative of the Lyapunov function is presented in (8):

$$\begin{aligned} \frac{\partial V}{\partial e_1} &= 2ae_1 - be_2 \\ \frac{\partial V}{\partial e_2} &= -be_1 + 2ce_2 \end{aligned} \tag{8}$$

Therefore, the derivative of the Lyapunov function $\dot{V}(e_1, e_2)$ can be obtained in (9), as shown at the bottom of the page.

In order to simplify the analysis of (9), assumptions are made in (10):

$$\begin{aligned} X &= 2ah_1 - bh_2 \\ Y &= \left(\frac{4a}{C_s}|e_1|^{\frac{1}{2}} - 2ch_2 + bh_1\right)|e_1|^{-\frac{1}{4}} \\ Z &= \frac{4b}{C_s} \end{aligned} \tag{10}$$

$$\begin{aligned} \dot{V}(e_1, e_2) &= \frac{\partial V}{\partial e_1}\dot{e}_1 + \frac{\partial V}{\partial e_2}\dot{e}_2 \\ &= (2ae_1 - be_2)\left(-h_1|e_1|^{\frac{1}{2}}\mathrm{sgn}(e_1) + \frac{2}{C_s}e_2\right) + (-be_1 + 2ce_2)\left(-k_{max} - h_2|e_1|^{\frac{1}{2}}\mathrm{sgn}(e_1)\right) \\ &= -2ah_1|e_1|^{\frac{3}{2}} + bh_1|e_1|^{\frac{1}{2}}e_2\mathrm{sgn}(e_1) + \frac{4a}{C_s}e_1e_2 - \frac{4b}{C_s}e_2^2 + bh_2|e_1|^{\frac{3}{2}} - 2ch_2|e_1|^{\frac{1}{2}}e_2\mathrm{sgn}(e_1) - k_{max}(-be_1 + 2ce_2) \\ &= -(2ah_1 - bh_2)|e_1|^{\frac{3}{2}} + \left[\left(\frac{4a}{C_s}|e_1|^{\frac{1}{2}} - 2ch_2 + bh_1\right)|e_1|^{-\frac{1}{4}}\right]|e_1|^{\frac{3}{4}}e_2\mathrm{sgn}(e_1) - \frac{4b}{C_s}e_2^2 - k_{max}(-be_1 + 2ce_2) \end{aligned} \tag{9}$$

By substituting (10) into (9), the equation for derivative of the Lyapunov function $\dot{V}(e_1, e_2)$ can be rewritten as (11):

$$\begin{aligned}\dot{V}(e_1,e_2) &= -X|e_1|^{\frac{3}{2}} + Y|e_1|^{\frac{3}{4}}e_2\mathrm{sgn}(e_1) \\ &\quad -Ze_2^2 - k_{max}(-be_1+2ce_2) \\ &= -X\left(|e_1|^{\frac{3}{4}}\right)^2 + Y|e_1|^{\frac{3}{4}}e_2\mathrm{sgn}(e_1) \\ &\quad -Ze_2^2 - k_{max}(-be_1+2ce_2) \\ &= -\left[X\left(|e_1|^{\frac{3}{4}}\right)^2 - Y|e_1|^{\frac{3}{4}}e_2\mathrm{sgn}(e_1) + Ze_2^2\right] \\ &\quad -k_{max}(-be_1+2ce_2) \\ &= V_1 - V_2 \end{aligned} \tag{11}$$

where

$$V_1 = -\left[X\left(|e_1|^{\frac{3}{4}}\right)^2 - Y|e_1|^{\frac{3}{4}}e_2\mathrm{sgn}(e_1) + Ze_2^2\right]$$

is a quadratic function with respect to $|e_1|^{\frac{3}{4}}\mathrm{sgn}(e_1)$ and e_2 while $V_2 = (-bk_{max}e_1 + 2ck_{max}e_2)$ is a plane function with respect to e_1 and e_2.

In order to obtain a negative semidefinite of $\dot{V}(e_1, e_2)$, the quadratic function V_1 must be designed to be negative definite in the first place. Therefore, the V_1 can be further expressed as (12):

$$\begin{aligned} V_1 &= -\left[X\left(|e_1|^{\frac{3}{4}}\right)^2 - Y|e_1|^{\frac{3}{4}}e_2\mathrm{sgn}(e_1) + Ze_2^2\right] \\ &= -\{X\left[\left(|e_1|^{\frac{3}{4}}\right)^2 - 2\frac{Y}{2X}|e_1|^{\frac{3}{4}}e_2\mathrm{sgn}(e_1) + \frac{Y^2}{4X^2}(e_2)^2\right] \\ &\qquad -\frac{Y^2}{4X}(e_2)^2 + Z(e_2)^2\} \\ &= -\left[X\left(|e_1|^{\frac{3}{4}} - \frac{Y}{2X}e_2\right)^2 + \left(Z - \frac{Y^2}{4X}\right)(e_2)^2\right] \end{aligned} \tag{12}$$

In (12), the $\left(|e_1|^{\frac{3}{4}} - \frac{Y}{2X}e_2\right)^2$ term is a positive semi-definite function and $(e_2)^2$ is a positive semi-definite function. Therefore, in order to guarantee V_1 to be a negative semi-definite function, following rules of X, Y and Z must be followed:

$$\begin{aligned} &(\mathbf{RULE3})X > 0 \\ &(\mathbf{RULE4})Z > \frac{Y^2}{4X} > 0 \end{aligned}$$

Following relationship in selecting parameters a, b, c, h_1 and h_2 can be obtained by RULE 3 and RULE 4:

From RULE 3:

- $X > 0 \rightarrow 2ah_1 - bh_2 > 0 \rightarrow 2ah_1 > bh_2$

From RULE4:

- $Z > 0 \rightarrow \frac{4b}{C_s} > 0 \rightarrow b > 0$
- $4XZ > Y^2$

In order to obtain the parameter relationship in $4XZ > Y^2$, Equation (13) is obtained by substituting (10) into an inequality of $4XZ > Y^2$:

$$4(2ah_1 - bh_2)\frac{4b}{C_s} > \left[\left(\frac{4a}{C_s}|e_1|^{\frac{1}{2}} - 2ch_2 + bh_1\right)|e_1|^{-\frac{1}{4}}\right]^2 \tag{13}$$

By rearranging (14), a new expression is presented in (14):

$$2\sqrt{(2ah_1 - bh_2)\frac{4b}{C_s}}|e_1|^{\frac{1}{4}} > \frac{4a}{C_s}|e_1|^{\frac{1}{2}} - 2ch_2 + bh_1 \tag{14}$$

Here, another assumption is made to simplify the analysis, as shown in (15):

$$\begin{aligned} U &= \frac{4a}{C_s} \\ V &= 2\sqrt{(2ah_1 - bh_2)\frac{4b}{C_s}} \\ W &= -2ch_2 + bh_1 \\ e_{new} &= |e_1|^{\frac{1}{4}} \end{aligned} \tag{15}$$

Substituting (15) into (14), the expression can be written using a new state e_{new} shown as (16):

$$Ve_{new} > U(e_{new})^2 + W \tag{16}$$

Since $U = \frac{4a}{C_s} > 0$, the expression $U(e_{new})^2 - Ve_{new} + W$ is a quadratic function going upwards. In order to make sure that there exist some meaningful areas that satisfy $V_1 < 0$, the vertex of the quadratic function must be smaller than zero so that the $U(e_{new})^2 - Ve_{new} + W$ has negative values. Additionally, in order to maximize the system stable region, the vertex of the quadratic function $U(e_{new})^2 - Ve_{new} + W$ is designed to be far less than 0. Considering the fact that for a practical power converter system, errors e_1, e_2 and e_{new} must be bounded due to system voltage and power limit, there exist meaningful parameters U, V and W that guarantees $U(e_{new})^2 - Ve_{new} + W < 0$. The vertex of the quadratic function (16) is related to $4UW - V^2$ and is designed to be much smaller than 0. Thus, (17) can be obtained by substituting (15) into an inequality of $4UW - V^2$ so that Rule 5 is obtained.

$$\begin{aligned} &4UW - V^2 \ll 0 \\ &\rightarrow 4(2ah_1 - bh_2)\frac{4b}{C_s} - 4\frac{4a}{C_s}(-2ch_2 + bh_1) \gg 0 \\ &\qquad \rightarrow a(bh_1 + 2ch_2) \gg b^2h_2 \end{aligned} \tag{17}$$

$$(\mathbf{RULE5})a(bh_1 + 2ch_2) \gg b^2h_2$$

Therefore, by following RULEs 1∼5, reasonable parameters a, b, c, h_1 and h_2 can be selected for the proposed nonlinear observer.

B. STABILITY OF THE PROPOSED NONLINEAR OBSERVER

Based on the observer parameters a, b, c, h_1 and h_2 which are selected following RULE 1-5, the stability of the proposed nonlinear observer can be determined by the Lyapunov

stability theory. Here, the positive definite of the Lyapunov function (6) is fulfilled based on RULE 1-2. The proposed nonlinear observer can be determined to be stable if and only if the derivative of the Lyapunov function is a negative semi-definite function. Based on (9)-(11), the polarity of $\dot{V}(e_1, e_2)$ can then be determined by the position relationship of the quadratic function V_1 and the plane function V_2 with given observer parameters a, b, c, h_1, h_2. The position relationship of both V_1 and V_2 with respect to e_1 and e_2 is shown in Fig. 2, where Fig. 2(a) presents the position relation of V_1 and V_2 during steady-state operation ($k = 0$) and Fig. 2(b) presents the position relation of V_1 and V_2 during an input power transience ($k > 0$).

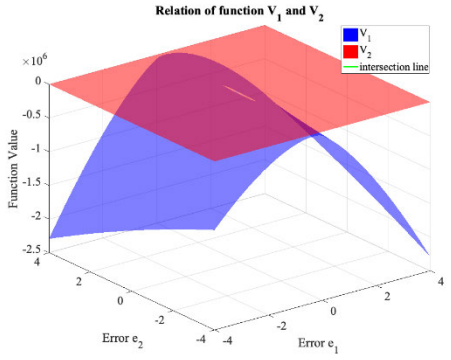

(a)

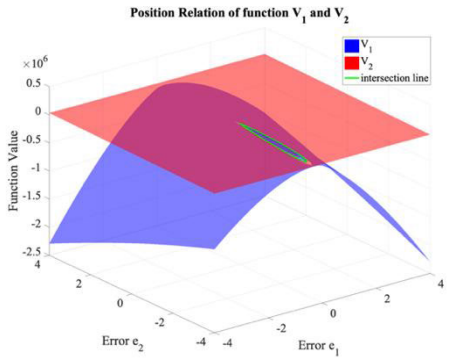

(b)

FIGURE 2. Position relationship of function V_1 and V_2. (a) during steady-state operation $k = 0$. (b) during input power transience $k > 0$.

As illustrated in (11) and (12), for given parameters of a, b, c, h_1 and h_2, the quadratic function V_1 is negative semi-definite with the largest value of 0. Meanwhile, the plane function V_2 has a slope k. As presented in Fig. 2(a), during steady-state operations where $k = 0$, the function $\dot{V}(e_1, e_2) \leq 0$ is always satisfied since the position of the function V_1 is always below the position of the function V_2, and the nonlinear observer is globally stable which has a positive definite Lyapunov function and its derivative is a negative semi-definite function ($V(e_1, e_2) > 0, \dot{V}(e_1, e_2) \leq 0$) for any e_1 and e_2. However, during input power transients where $k \neq 0$, there exists an intersection area, which is represented by the green circle in Fig. 2(b). The green intersection line of V_1 and V_2 represents the area where $V_1 = V_2$. In other word, function $\dot{V}(e_1, e_2) = 0$. The area outside the intersection region is the area where $V_1 < V_2$ which means function $\dot{V}(e_1, e_2) = V_1 - V_2 < 0$. According to the Lyapunov stability theory, the proposed nonlinear observer is stable in this area ($V(e_1, e_2) > 0, \dot{V}(e_1, e_2) < 0$). Meanwhile, the area inside the intersection line, where $V_1 > V_2$, is the part that does not satisfied the negative definite condition ($\dot{V}(e_1, e_2) > 0$), which means that the proposed observer would not be stable within this region. Even though there exists an area that does not satisfy the Lyapunov stability condition around the origin, the nonlinear observer is still determined to be stable globally according to the Lyapunov stability theory. The state errors e_1 and e_2 would converge to this intersection line in the neighborhood of the origin instead of converging to the origin. However, this convergence phenomenon may lead to estimation oscillations in practices, which may require further modifications. Meanwhile, based on mathematical analysis, the larger the parameters h_1 and h_2 are selected, the smaller this unstable neighborhood is. Thus, for the propose nonlinear observer design for a practical power conversion system, reasonable large gains h_1 and h_2 can be selected to achieve a desire observer performance and to minimize the unstable region and estimation oscillations.

C. PROPOSED NONLINEAR CONTROL ALGORITHM

The proposed nonlinear power decoupling control algorithm is obtained by combining the proposed nonlinear power observer with a conventional PI controller. The block diagram of the proposed control method is presented in Fig. 3, where V_{dcref} represents the DC-link voltage reference, i_{qref} is the calculated reference for the q-axis current, K_{con} is a parameter-dependent gain of the control system, L_s represents the nominal inductance of the grid-side filter, V_q and i_q represent the q-axis grid voltage and current in the d-q rotating reference frame, u_{out} is the generated system control output, s is the integral operator, R_s is the grid filter resistance which is usually very small and can be neglected, $\hat{p}_{in}^N$ is the estimated input power from the proposed nonlinear observer and i_{comp} represents the feedforward compensation current generated by the proposed observer. As discussed in [39], [40], the DC-link voltage control can be aligned with either d-axis or q-axis depending on the phase angle used for Park's transformation during controller design. In this paper, the DC-link voltage control is aligned with q-axis. Meanwhile the reactive power control is aligned with d-axis and is neglected when a unity power factor is applied. The mathematical process of proposed nonlinear observer is shown in Fig. 4.

As shown in Fig. 4, system output $y[K] = V_{dc}^2[K]$ and system control input $u[K] = p_{out}^N[K]$ are first obtained through calculations of the measured DC-link voltage, grid voltage and current in the K_{th} interval. Meanwhile, estimated variables $\hat{y}[K-1]$, $\hat{x}_1[K-1]$ and $\hat{x}_2[K-1]$ are obtained from the calculations in $(K\text{-}1)_{\text{th}}$ interval. And the error variable $e[K]$ can then be processed with $e[K] = \hat{y}[K-1] - y[K]$. The estimated values $\hat{x}_1[K]$ and $\hat{x}_2[K]$ at the k_{th} interval

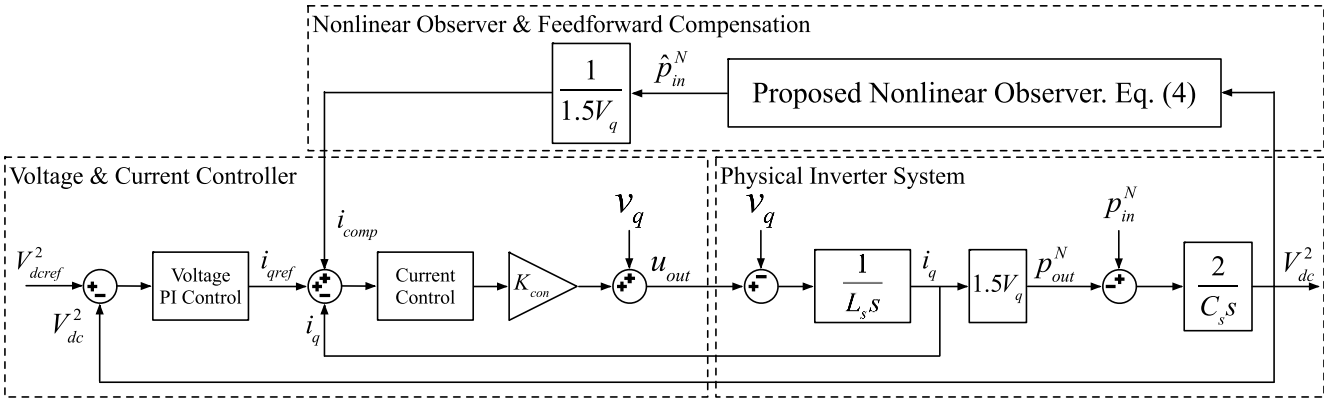

FIGURE 3. Block diagram of the proposed nonlinear control algorithm.

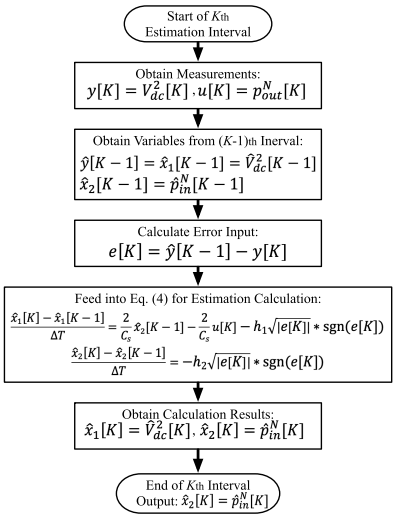

FIGURE 4. Detailed calculation of the estimated DC-link input power.

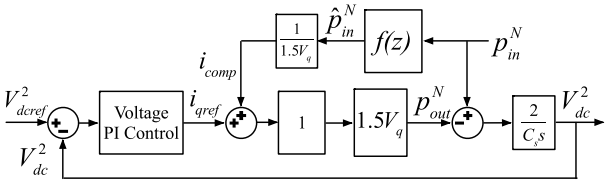

FIGURE 5. Simplified block diagram of the proposed nonlinear control algorithm.

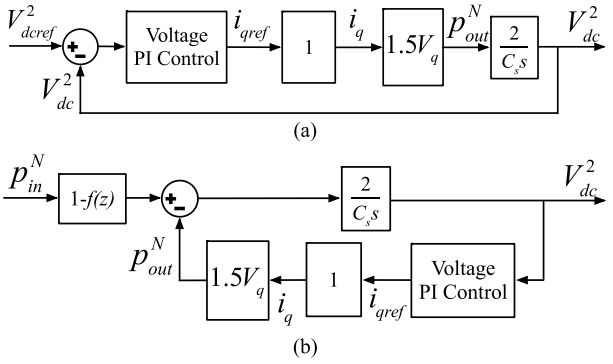

FIGURE 6. Rearranged block diagram of the proposed nonlinear control algorithm. (a) Block diagram for reference tracking. (b) Block diagram for disturbance rejection.

are calculated by integrating all variables $e[K]$, $\hat{x}_1[K-1]$, $\hat{x}_2[K-1]$ and $u[K]$ into the discrete-time equation of Eq. (4). Therefore, the estimated input power $\hat{p}_{in}^N[K]$ can be calculated from $\hat{p}_{in}^N[K] = \hat{x}_2[K]$ through Eq. (4). Here, ΔT is the time duration between two adjacent estimation intervals.

Then, in order to analyze the performance of the proposed controller, simplifications are made on the block diagram based on following assumptions: 1. The inner q-axis current loop is usually designed to have very fast transient performance and is assumed to be ideal with a unity gain when investigating the performance of the slow voltage control loop; and 2. A nonlinear function $\frac{\hat{p}_{in}^N}{p_{in}^N} = f(z)$ is used to represent the behavior of the proposed nonlinear observer. The simplified block diagram can be obtained in Fig. 5 where the inner current control loop is represented by a unit block.

By rearranging the blocks in Fig. 5, the block diagrams for reference tracking and for disturbance rejection can be obtained in Fig. 6 where Fig. 6(a) represents the behavior of the proposed algorithm in tracking DC-link voltage reference while Fig. 6(b) illustrates the performance of the proposed method under rapid input power variations.

As illustrated in Fig. 6(a), the proposed nonlinear observer does not affect the performance when tracking a given voltage reference since it is irrelevant to this block diagram. The performance and the stability criteria of the proposed algorithm in reference tracking relies on the voltage PI controller. Meanwhile, the proposed observer is capable of minimizing DC-link voltage fluctuations when analyzing disturbance rejection, as shown in Fig. 6(b). The disturbance p_{in}^N is sent through a prefilter $(1 - f(z))$ before being processed in the voltage loop. And the faster the nonlinear observer is designed $f(z) \rightarrow 1$, the smaller the impact of p_{in}^N on the

DC-link voltage. Here, the stability criteria of the disturbance rejection block diagram are determined by both the nonlinear observer and the voltage PI controller.

IV. SIMULATION AND EXPERIMENTAL RESULTS

In order to verify the effectiveness of the proposed nonlinear DC-link voltage control and the improvement over other voltage control methods, results from both simulation on a MATLAB/SIMULINK platform and experimental tests through a prototype DER power conversion system are discussed in this section by comparing the performance of the proposed nonlinear controller with an observer-based controller presented in [33] as a reference method. The system parameters for both the MATLAB/SIMULINK-based simulation platform and the experiment prototype are summarized in Table 1.

TABLE 1. Parameters for hybrid DER power inverter.

Parameter	Value
DC-link voltage reference V_{dcref}	400V
Three-phase grid voltage	208V
q-axis grid voltage V_q	169V
DC-link capacitor C_s	1100uF
Grid filter inductance L_s	1.8mH
Grid filter resistance R_s	Too small, ignored
Power rating	14kW
Switching frequency	10kHz
Maximum power changing rate k	5000000 W/s
Observer gain h_1	2000
Observer gain h_2	50000

Remark 1: The proposed nonlinear observer is built based on an assumption that in a practical power converter application, the changing rate of the input power is bounded with a maximum value of k. Therefore, a ramp function, instead of a step function, is used on the simulation platform to simulate input power changes.

Remark 2: The PI parameters in both the proposed method and the reference method are selected to be identical and are tuned to meet the standardized regulations for the harmonics content in the DER power converter during steady-state operations.

Remark 3: Considering the fact that the use of sign function $sgn(e)$ in the proposed method will results in steady-state control chattering and high current THD issues. A saturation function $sat(e)$ is used in the proposed method for both simulation and experimental tests to achieve an improvement of the steady-state performance of the proposed controller.

A. SIMULATION RESULTS

The simulation verification of the proposed nonlinear DC-link control algorithm is obtained by comparing the DC-link performance of the proposed method with a reference method presented by [33] during input power transience. The performance of the proposed nonlinear observer and the controller is shown in Fig. 7 where there exists an input power ramp up from 2kW to 6kW at 0.1s and an input power ramp down from 6kW to 2kW at 0.2s. And the performance of both control methods is summarized in Table 2.

TABLE 2. Summary of the simulation results.

	Proposed Method	Reference Method
Simulation Results		
Estimation settling time	10ms	10ms
Estimation steady-state error	100W	100W
Estimation steady-state oscillation	100W	180W
Maximum DC-link voltage variation	6V	6V
DC-link voltage settling time	50ms	50ms
DC-link voltage steady-state fluctuation	0.8V	0.9V
Grid current THD	2.84%	3.44%

As illustrated in Fig. 7(a), both the proposed method and the reference method are tuned with an almost identical DC-link voltage performance with a voltage variation of about 6V during input power step up change from 2kW to 6kW and during input power step down change from 6kW to 2kW, a settling time of 50ms and a steady-state voltage oscillation with a magnitude of less than 1V. With use of the saturation function of in proposed nonlinear observer and better parameters tuning of reference observer, both observers have achieved similar transient performance, as shown in Fig. 7(b), (c), with fast input power estimation of 10ms. However, when looking into the detailed performance of both methods, the proposed method has better steady-state performance with an estimation oscillation of 100W compared to 180W of reference observer, as presented in Fig. 7(d). Meanwhile, the inverter output active-reactive power performance of both method is shown in Fig. 7(e) where the proposed method has better performance with smaller active power overshoot and reactive power oscillation. Moreover, the grid current analysis in Fig. 7(f)-(h) reveals that the proposed method also has better current performance with smaller current THD of 2.84% compared to the reference method with 3.44%. In general, even though both methods have shown similar DC-link voltage performance, the proposed method has better power estimation compared to the reference method, which results in a better steady-state control performance with smaller current THD under an ideal grid condition.

B. EXPERIMENTAL RESULTS

The experiment validations have been carried out on a prototype DER power conversion system under practical grid conditions, as shown in Fig. 8, where Zone A is the DSP TMS320F28335 core control circuit; Zone B is the DC-link and three-phase grid-side inverter; and Zone C is the DER-side converters. Similar to the simulation verification, the performance of the investigated proposed method is compared to a reference method presented by [33]. Note: all the waveforms of the experimental results in Fig. 9-11 are captured by a HIOKI 8860-50 Memory Hicorder and are replotted in MATLAB. Two simulated DER are used as input sources to the experimental prototype: 1. An adjustable three-phase

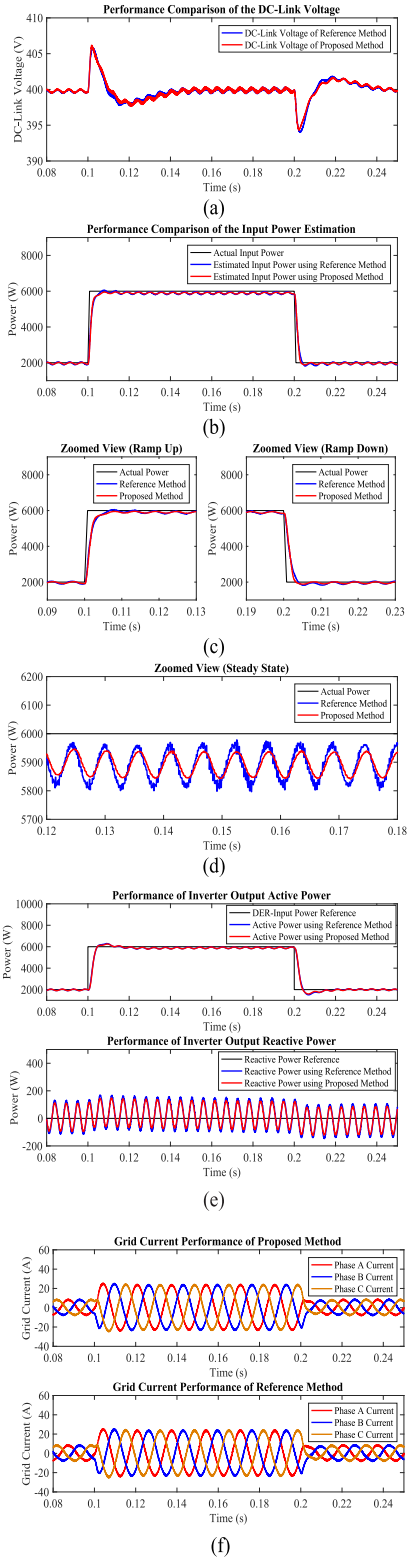

FIGURE 7. Simulation results of the proposed method compared with the reference method. (a) DC-link voltage performance comparison during input power changes. (b) Performance comparison of the input power estimation. (c) Zoomed view of the estimation during input power changes. (d) Zoomed view of the estimation during steady states. (e) Inverter output active-reactive power performance. (f) Grid current performance comparison during input power changes. (g) Measured grid current THD of proposed method. (h) Measured grid current THD of reference method.

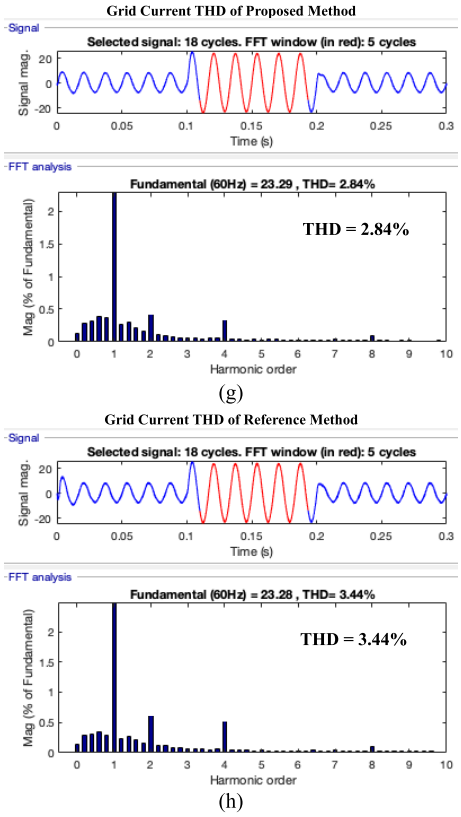

FIGURE 7. *(Continued.)* Simulation results of the proposed method compared with the reference method. (a) DC-link voltage performance comparison during input power changes. (b) Performance comparison of the input power estimation. (c) Zoomed view of the estimation during input power changes. (d) Zoomed view of the estimation during steady states. (e) Inverter output active-reactive power performance. (f) Grid current performance comparison during input power changes. (g) Measured grid current THD of proposed method. (h) Measured grid current THD of reference method.

voltage source which simulates a permanent magnet synchronous generator (PMSG) of a small-scale wind generation system. And 2. A Chroma 62000H programmable PV simulator which simulates the characteristic of PV panels. Both simulated sources are controlled by the DER-side converters for power extraction. Here, the PV is maintained with a constant power output while the voltage source has been controlled with step changes simulating sudden input power variation to the DC-link.

Considering the fact that the grid voltage will heavily affect performance of the output current particularly on current harmonics, the voltage waveform and its spectrum analysis are first presented in Fig. 9 for demonstrating practical limitations due to laboratory three-phase grid voltage distortion in experimental verification. Then experimental results of both the proposed method and reference method are presented in Fig. 10 and Fig. 11 where power changes are designed to have an input power ramp up from 2kW to 6kW and a power ramp down from 6kW to 2kW in experimental tests. Here, both methods are tuned with an almost identical DC-link voltage

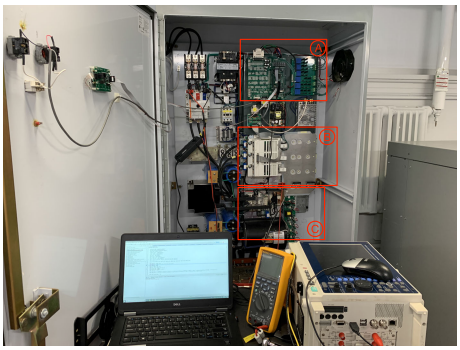

FIGURE 8. Prototype DER power conversion system.

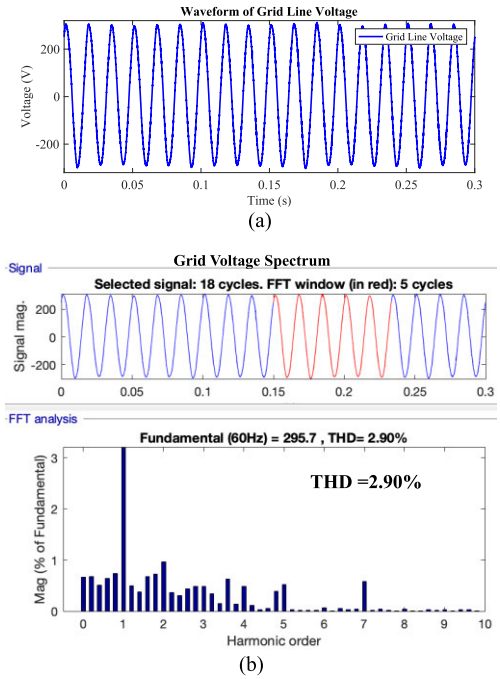

FIGURE 9. Grid voltage characteristics. (a) Waveform of grid line voltage. (b) Grid line voltage spectrum.

TABLE 3. Summary of the experimental results.

	Proposed Method	Reference Method
Experimental Results		
DC voltage variation (Step Up)	20V	20V
DC voltage variation (Step Down)	23V	30V
Settling time	20ms	50ms
DC-link voltage steady-state fluctuation	11V	10V
Current THD	3.98%	4.64%

variation of 20V during power step changes for performance comparison.

In order to demonstrate the improvement of the proposed method over the reference method, a summary of control performance based on experimental results is presented in Table 3.

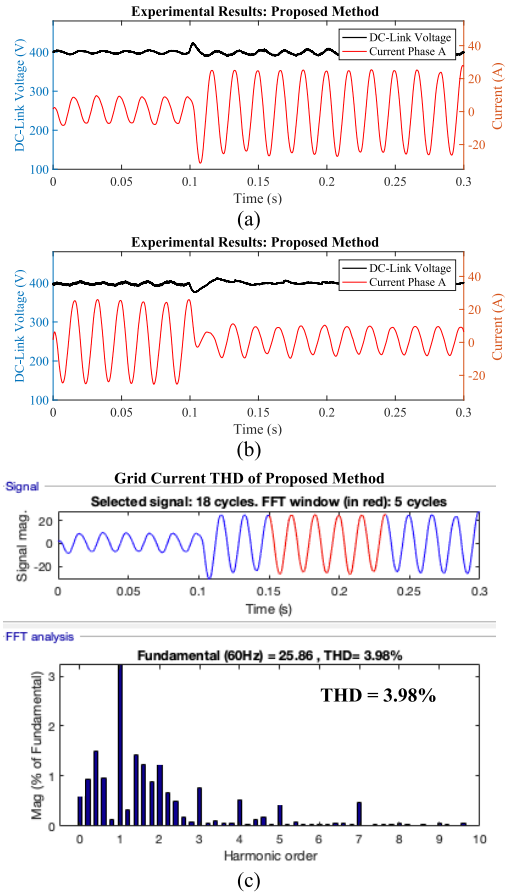

FIGURE 10. Experimental results of the proposed method. (a) DC-link voltage and grid current performance during input power ramp up. (b) DC-link and grid current performance during input power ramp down. (c) Grid current THD analysis.

As illustrated in Table 3, both control methods have almost identical DC-link voltage variations of 20V during a 4kW input power step up change. However, the proposed method has a faster settling time of 20ms, smaller grid current THD of 3.98% and similar steady-state voltage fluctuations of 11V, compared with 50ms settling time, current THD of 4.64% and 10V DC-link voltage steady-state fluctuation of the reference method, respectively. Meanwhile, as presented in Fig. 10(b) and Fig. 11(b), the proposed method not only has a better steady-state performance of faster settling time, smaller current THD, etc., but also has a smaller DC-link voltage variation of 23V during this 4kW input power step down change compared to a 30V voltage variation of reference method. However, even though the proposed method has shown better THD performance, it has shown some DC and even harmonics concerns as presented in Fig. 10(c). Although these harmonics are mainly caused by the grid voltage distortion, it is still required to determine whether current distortions have followed grid standards. According to IEEE 1547-2018, the inverter output current has individual harmonics requirement with Total Rated-current Distortion (TRD) limitation which has a different TRD calculation equation compared to the

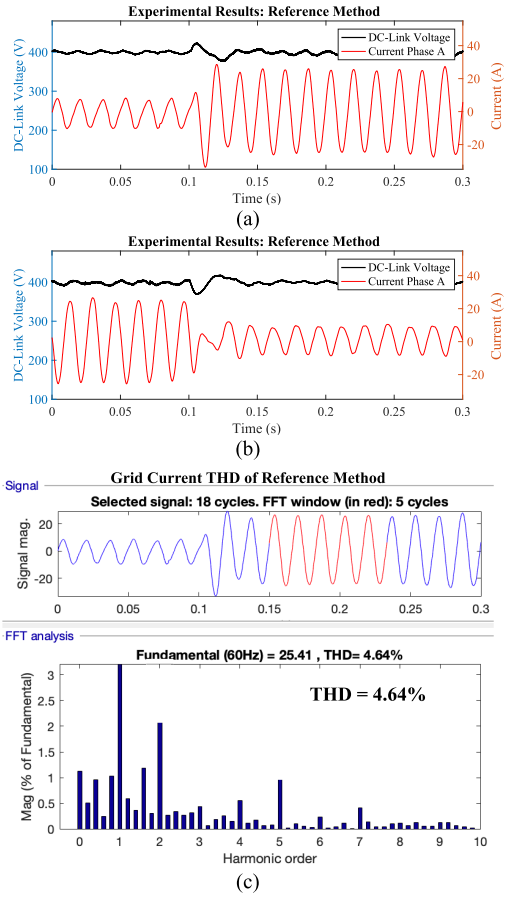

FIGURE 11. Experimental results of the reference method. (a) DC-link voltage and grid current performance during input power ramp up. (b) DC-link and grid current performance during input power ramp down. (c) Grid current THD analysis.

THD equation used in Fig. 10(c) in MATLAB. After performing TRD-THD conversion, we can conclude that these current distortions of each individual harmonics are within the TRD requirement in IEEE 1547-2018 for grid-connected operation.

Therefore, based on experimental results, it is clear that the proposed nonlinear DC-link voltage control method has a significant improvement on the DC-link transient performance over the reference method under practical grid conditions with rapid input power changes. And the proposed method has followed grid interconnection standard for practical applications.

V. CONCLUSION

In DER power conversion system applications, fast DC-link voltage regulation is necessary so that the grid-side inverter and the DER-side converter can be fully decoupled. Moreover, by maintaining a constant DC-link voltage, good transient and steady-state performance can be achieved. In this paper, a novel nonlinear control algorithm is proposed to perform rapid power estimation as well as to minimize the DC-link voltage fluctuation for DER power conversion systems. Compared with other typical controllers in recent literature, improvements in transient performance of the proposed nonlinear method have been verified in both simulations on a MATLAB/SIMULINK platform and experiments on a prototype DER power conversion system. The proposed nonlinear control method offers a faster DC-link voltage regulation capability and better performance during rapid power transience.

REFERENCES

[1] *Renewable Capacity Statistics 2019*, International Renewable Energy Agency (IRENA), IRENA, Abu Dhabi, United Arab Emirates, 2019.

[2] *Global Energy Transformation: A Roadmap to 2050*, International Renewable Energy Agency (IRENA), IRENA, Abu Dhabi, United Arab Emirates, 2018.

[3] *Renewable Energy Market Analysis: GCC 2019*, International Renewable Energy Agency (IRENA), IRENA, Abu Dhabi, United Arab Emirates, 2019.

[4] *Global Wind Report*, Global Wind Energy Council (GWEC), GWEC, Brussels, Belgium, 2019.

[5] A. JäGer-Waldau, *PV Status Report 2018*, JRC Science for Policy Report, Luxembourg, Luxembourg, 2018.

[6] *Battery Storage for Renewables: Market Status and Technology Outlook*, International Renewable Energy Agency (ARENA), IRENA, Ruud Kempener and Eric Borden, Abu Dhabi, United Arab Emirates, 2015.

[7] *Global EV Outlook 2018*, International Energy Agency (IEA), IEA, Paris, France, 2018.

[8] C. Lumbreras, J. M. Guerrero, P. Garcia, F. Briz, and D. D. Reigosa, "Control of a small wind turbine in the high wind speed region," *IEEE Trans. Power Electron.*, vol. 31, no. 10, pp. 6980–6991, Oct. 2016.

[9] V. Yaramasu, B. Wu, P. C. Sen, S. Kouro, and M. Narimani, "High-power wind energy conversion systems: State-of-the-art and emerging technologies," *Proc. IEEE*, vol. 103, no. 5, pp. 740–788, May 2015.

[10] E. Chatzinikolaou and D. J. Rogers, "A comparison of grid-connected battery energy storage system designs," *IEEE Trans. Power Electron.*, vol. 32, no. 9, pp. 6913–6923, Sep. 2017.

[11] M. Vasiladiotis and A. Rufer, "A modular multiport power electronic transformer with integrated split battery energy storage for versatile ultrafast EV charging stations," *IEEE Trans. Ind. Electron.*, vol. 62, no. 5, pp. 3213–3222, May 2015.

[12] C. Wang, X. Li, L. Guo, and Y. W. Li, "A nonlinear-disturbance-observer-based DC-bus voltage control for a hybrid AC/DC microgrid," *IEEE Trans. Power Electron.*, vol. 29, no. 11, pp. 6162–6177, Nov. 2014.

[13] Y. Zhang, J. Wang, and Z. Li, "Uncertainty modeling of distributed energy resources: Techniques and challenges," *Current Sustain. Energy Rep.*, vol. 6, no. 2, pp. 42–51, Jun. 2019.

[14] B. Cao, L. Chang, and R. Shao, "A simple approach to current THD prediction for small-scale grid-connected inverters," in *Proc. IEEE Appl. Power Electron. Conf. Expo. (APEC)*, Mar. 2015, pp. 3348–3352.

[15] A. Navarro-Rodriguez, P. Garcia, R. Georgious, and J. Garcia, "Adaptive active power sharing techniques for DC and AC voltage control in a hybrid DC/AC microgrid," *IEEE Trans. Ind. Appl.*, vol. 55, no. 2, pp. 1106–1116, Mar. 2019.

[16] H. Wen, W. Xiao, X. Wen, and P. Armstrong, "Analysis and evaluation of DC-link capacitors for high-power-density electric vehicle drive systems," *IEEE Trans. Veh. Technol.*, vol. 61, no. 7, pp. 2950–2964, Sep. 2012.

[17] J. M. Espi and J. Castello, "Wind turbine generation system with optimized DC-link design and control," *IEEE Trans. Ind. Electron.*, vol. 60, no. 3, pp. 919–929, Mar. 2013.

[18] N. Hur, J. Jung, and K. Nam, "A fast dynamic DC-link power-balancing scheme for a PWM converter-inverter system," *IEEE Trans. Ind. Electron.*, vol. 48, no. 4, pp. 794–803, Aug. 2001.

[19] Y. Tian, Z. Chen, F. Deng, X. Sun, and Y. Hu, "Active power and DC voltage coordinative control for cascaded DC–AC converter with bidirectional power application," *IEEE Trans. Power Electron.*, vol. 30, no. 10, pp. 5911–5925, Oct. 2015.

[20] P. Alemi, Y.-C. Jeung, and D.-C. Lee, "DC-link capacitance minimization in T-type three-level AC/DC/AC PWM converters," *IEEE Trans. Ind. Electron.*, vol. 62, no. 3, pp. 1382–1391, Mar. 2015.

[21] L. Yin, Z. Zhao, T. Lu, S. Yang, and G. Zou, "An improved DC-link voltage fast control scheme for a PWM rectifier-inverter system," *IEEE Trans. Ind. Appl.*, vol. 50, no. 1, pp. 462–473, Jan. 2014.
[22] M. Bagheri-Farahbakhsh, A. Cross, D. Strickland, P. Morris, T. Martin, and T. Lakin, "Hybrid PV/battery-storage unit for residential applications," *J. Eng.*, vol. 2019, no. 17, pp. 3532–3536, Jun. 2019.
[23] R. Pena-Alzola, D. Campos-Gaona, P. F. Ksiazek, and M. Ordonez, "DC-link control filtering options for torque ripple reduction in low-power wind turbines," *IEEE Trans. Power Electron.*, vol. 32, no. 6, pp. 4812–4826, Jun. 2017.
[24] A. Tazay and Z. Miao, "Control of a three-phase hybrid converter for a PV charging station," *IEEE Trans. Energy Convers.*, vol. 33, no. 3, pp. 1002–1014, Sep. 2018.
[25] C. Jain and B. Singh, "A three-phase grid tied SPV system with adaptive DC link voltage for CPI voltage variations," *IEEE Trans. Sustain. Energy*, vol. 7, no. 1, pp. 337–344, Jan. 2016.
[26] M. Merai, M. W. Naouar, and I. Slama-Belkhodja, "An improved DC-link voltage control strategy for grid connected converters," *IEEE Trans. Power Electron.*, vol. 33, no. 4, pp. 3575–3582, Apr. 2018.
[27] J. Honkanen, J. Hannonen, J. Korhonen, N. Nevaranta, and P. Silventoinen, "Nonlinear PI-control approach for improving the DC-link voltage control performance of a power-factor-corrected system," *IEEE Trans. Ind. Electron.*, vol. 66, no. 7, pp. 5456–5464, Jul. 2019.
[28] C.-Y. Tang, Y.-F. Chen, Y.-M. Chen, and Y.-R. Chang, "DC-link voltage control strategy for three-phase back-to-back active power conditioners," *IEEE Trans. Ind. Electron.*, vol. 62, no. 10, pp. 6306–6316, Oct. 2015.
[29] A. Merabet, K. T. Ahmed, H. Ibrahim, and R. Beguenane, "Implementation of sliding mode control system for generator and grid sides control of wind energy conversion system," *IEEE Trans. Sustain. Energy*, vol. 7, no. 3, pp. 1327–1335, Jul. 2016.
[30] A. Rodriguez-Cabero, M. Prodanovic, and J. Roldan-Perez, "Full-state feedback control of back-to-back converters based on differential and common power concepts," *IEEE Trans. Ind. Electron.*, vol. 66, no. 11, pp. 9045–9055, Nov. 2019.
[31] M. Gupta and G. Venkataramanan, "Robust predictive control of high-density cascaded DC voltage link power converters," *IEEE J. Emerg. Sel. Topics Power Electron.*, vol. 7, no. 4, pp. 2213–2224, Dec. 2019.
[32] J. Liu, S. Vazquez, L. Wu, A. Marque, H. Gao, and L. G. Franquelo, "Extended state observer-based sliding-mode control for three-phase power converters," *IEEE Trans. Ind. Electron.*, vol. 64, no. 1, pp. 22–31, Jan. 2017.
[33] J. Lu, S. Golestan, M. Savaghebi, J. C. Vasquez, J. M. Guerrero, and A. Marzabal, "An enhanced state observer for DC-link voltage control of three-phase AC/DC converters," *IEEE Trans. Power Electron.*, vol. 33, no. 2, pp. 936–942, Feb. 2018.
[34] M. Merai, M. W. Naouar, I. Slama-Belkhodja, and E. Monmasson, "An improved DC-link voltage control for a three-phase PWM rectifier using an adaptive PI controller combined with load current estimation," in *Proc. 19th Eur. Conf. Power Electron. Appl. (EPE ECCE Eur.)*, Sep. 2017, pp. 1–10.
[35] G. Song, B. Cao, L. Chang, R. Shao, and S. Xu, "A novel DC-link voltage control for small-scale grid-connected wind energy conversion system," in *Proc. IEEE Appl. Power Electron. Conf. Expo. (APEC)*, Mar. 2019, pp. 2461–2466.
[36] G. Song, B. Cao, L. Chang, and R. Shao, "A novel adaptive observer-based DC-link voltage control for grid-connected power converters," in *Proc. IEEE 10th Int. Symp. Power Electron. Distrib. Gener. Syst. (PEDG)*, Jun. 2019, pp. 604–610.
[37] G. Song, B. Cao, L. Chang, and R. Shao, "Novel nonlinear DC-link voltage control for small-scale grid-connected wind power converters," in *Proc. 10th Int. Conf. Power Electron. ECCE Asia (ICPE-ECCE Asia)*, May 2019, pp. 1–6.
[38] H. Hu, S. Harb, N. Kutkut, I. Batarseh, and Z. J. Shen, "A review of power decoupling techniques for microinverters with three different decoupling capacitor locations in PV systems," *IEEE Trans. Power Electron.*, vol. 28, no. 6, pp. 2711–2726, Jun. 2013.
[39] S.-H. Hwang, L. Liu, H. Li, and J.-M. Kim, "DC offset error compensation for synchronous reference frame PLL in single-phase grid-connected converters," *IEEE Trans. Power Electron.*, vol. 27, no. 8, pp. 3467–3471, Aug. 2012.
[40] X. Zhou, Q. Liu, Y. Ma, and B. Xie, "DC-link voltage research of photovoltaic grid-connected inverter using improved active disturbance rejection control," *IEEE Access*, vol. 9, pp. 9884–9894, 2021.

GUANHONG SONG (Member, IEEE) received the B.Sc. degree in electrical engineering from Southwest Jiaotong University, Chengdu, China, in 2013, and the Ph.D. degree from the University of New Brunswick, Fredericton, NB, Canada, in 2020. He is currently a Postdoctoral Fellow with the Emera and NB Power Research Centre for Smart Grid Technologies, University of New Brunswick. His current research interests include power electronics, power converters, and distributed generation systems.

BO CAO (Member, IEEE) received the B.Sc. degree in electronic from the East China University of Science and Technology, Shanghai, China, in 2005, and the Ph.D. degree from the University of New Brunswick, Fredericton, NB, Canada, in 2015. He is currently a Research Associate with the Emera and NB Power Research Centre for Smart Grid Technologies, University of New Brunswick. His research interests include power converter design, grid-integration technology, distributed generation systems, and smart grid techniques.

LIUCHEN CHANG (Senior Member, IEEE) received the B.Sc. degree in electrical engineering (E.E.) from Northern Jiaotong University, in 1982, the M.Sc. degree from the China Academy of Railway Sciences, in 1984, and the Ph.D. degree from Queen's University, in 1991. In 1992, he joined the University of New Brunswick (UNB). He is currently a Professor Emeritus at UNB. He has published more than 400 refereed papers in journals and conference proceedings. Specializing in power electronics, he has focused on research, development, demonstration and deployment of renewable energy-based distributed energy systems, and direct load control systems. He is a fellow of the Canadian Academy of Engineering (FCAE). He is a long-time volunteer for IEEE of over 28 years and the President of the IEEE Power Electronics Society, from 2021 to 2022.

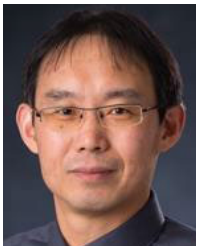

RIMING SHAO (Member, IEEE) received the B.Sc. degree in electrical engineering (E.E.) and the M.Sc. degree from Tongji University, Shanghai, China, in 1994 and 1997, respectively, and the Ph.D. degree from the University of New Brunswick, Fredericton, NB, Canada, in 2010. He is currently working as a Project Engineer with Alpha Technologies Inc., Bellingham, WA, USA. His research interests include smart grids, power converters, renewable energy systems, and distributed power generation systems. He is a Registered Professional Engineer of APEGNB, Canada.